SARS-CoV-2 pathogenesis in an angiotensin II–induced heart-on-a-chip disease model and extracellular vesicle screening

Wu, Qinghua; Rafatian, Naimeh; Wagner, Karl T.; Blamer, Jacob; Smith, Jacob; Okhovatian, Sargol; Aggarwal, Praful; Wang, Erika Yan; Banerjee, Arinjay; Zhao, Yimu; Nash, Trevor R.; Lu, Rick Xing Ze; Portillo-Esquivel, Luis Eduardo; Li, Chen Yu; Kuzmanov, Uros; Mandla, Serena; Virlee, Elizabeth; Landau, Shira; Lai, Benjamin Fook; Gramolini, Anthony O.; Liu, Chuan; Fleischer, Sharon; Veres, Teodor; Vunjak-Novakovic, Gordana; Zhang, Boyang; Mossman, Karen; Broeckel, Ulrich; Radisic, Milica

Publisher's version / Version de l'éditeur:
https://doi.org/10.1073/pnas.2403581121
Proceedings of the National Academy of Sciences, 121, 28, pp. 1-11, 2024-07-05

PNAS RESEARCH ARTICLE | APPLIED BIOLOGICAL SCIENCES ENGINEERING OPEN ACCESS

SARS-CoV-2 pathogenesis in an angiotensin II–induced heart-on-a-chip disease model and extracellular vesicle screening

Qinghua Wu[a,b], Naimeh Rafatian[a], Karl T. Wagner[a,c], Jacob Blamer[e], Jacob Smith[c], Sargol Okhovatian[a,b], Praful Aggarwal[e], Erika Yan Wang[a], Arinjay Banerjee[f,g], Yimu Zhao[h], Trevor R. Nash[h], Rick Xing Ze Lu[a], Luis Eduardo Portillo-Esquivel[i], Chen Yu Li[c], Uros Kuzmanov[j,k], Serena Mandla[b], Elizabeth Virlee[e], Shira Landau[a], Benjamin Fook Lai[a], Anthony O. Gramolini[j,k], Chuan Liu[a,b,m], Sharon Fleischer[h], Teodor Veres[d,l], Gordana Vunjak-Novakovic[h,n], Boyang Zhang[i], Karen Mossman[f], Ulrich Broeckel[e], and Milica Radisic[a,b,c,m,1]

Affiliations are included on p. 10.

Edited by Lauren D. Black, Tufts University, Medford, MA; received February 20, 2024; accepted May 17, 2024 by Editorial Board Member Diane E. Griffin

Adverse cardiac outcomes in COVID-19 patients, particularly those with preexisting cardiac disease, motivate the development of human cell-based organ-on-a-chip models to recapitulate cardiac injury and dysfunction and for screening of cardioprotective therapeutics. Here, we developed a heart-on-a-chip model to study the pathogenesis of SARS-CoV-2 in healthy myocardium established from human induced pluripotent stem cell (iPSC)-derived cardiomyocytes and a cardiac dysfunction model, mimicking aspects of preexisting hypertensive disease induced by angiotensin II (Ang II). We recapitulated cytopathic features of SARS-CoV-2-induced cardiac damage, including progressively impaired contractile function and calcium handling, apoptosis, and sarcomere disarray. SARS-CoV-2 presence in Ang II–treated hearts-on-a-chip decreased contractile force with earlier onset of contractile dysfunction and profoundly enhanced inflammatory cytokines compared to SARS-CoV-2 alone. Toward the development of potential therapeutics, we evaluated the cardioprotective effects of extracellular vesicles (EVs) from human iPSC which alleviated the impairment of contractile force, decreased apoptosis, reduced the disruption of sarcomeric proteins, and enhanced beta-oxidation gene expression. Viral load was not affected by either Ang II or EV treatment. We identified MicroRNAs miR-20a-5p and miR-19a-3p as potential mediators of cardioprotective effects of these EVs.

organ-on-a-chip | SARS-CoV-2 | cardiomyocyte | induced pluripotent stem cell | myocardium

Significance

This study presents a disease model that simulates cardiac function in hypertensive heart disease patients, who are more severely impacted by severe acute respiratory syndrome coronavirus-2 (SARS-CoV-2). This model offers insight into the functional and molecular differences between healthy and hypertensive-like myocardium in the presence of SARS-CoV-2, facilitating the screening of biologics such as extracellular vesicles. It could pave the way for identifying advanced therapeutics for hypertensive heart disease in inflammatory conditions.

Cardiac complications have been noted in up to 62% of COVID-19 patients, with higher risks in those with preexisting conditions such as hypertension (1–3). Genetically modified mice can be used to model SARS-CoV-2-induced cardiac dysfunction (4). Yet animal models fail to sufficiently mimic human tissue-specific pathophysiological processes and suffer from low affinity of the SARS-CoV-2 spike protein for the ACE2 receptor (5). Models based on human induced pluripotent stem cell (iPSC) may be better suited (6–8), but those incorporating existing cardiac conditions are scarce.

Given the established causal relationship between angiotensin II (Ang II) and the onset of hypertensive heart disease (9), its increase in plasma of COVID-19 patients (10), and its role in the advancement of chronic heart failure (11), we used an Ang II–conditioned heart-on-a-chip to simulate SARS-CoV-2 infection superimposed on an existing cardiac condition. Previously, the application of Ang II, the main peptide of the renin-angiotensin system (RAS), has been reported to successfully model nongenetic cardiomyopathy (12, 13). The RAS is crucial in mediating cardiovascular responses in the context of COVID-19 pathogenesis (14).

The multifaceted effects of SARS-CoV-2 infection in the heart may require mechanistic understanding of therapies acting on multiple pathways, such as those provided by extracellular vesicles (EVs) and their microRNA (miRNA) (15–18). Here, in conjunction with mapping cytokine secretion and gene expression, the capacity for long-term tissue culture and real-time contractile function readouts of the heart-on-a-chip allowed us to quantify the extent of cardiac dysfunction upon SARS-CoV-2 application. SARS-CoV-2 presence in Ang II–treated hearts-on-a-chip exacerbated the earlier onset of contractile dysfunction and profoundly enhanced inflammatory cytokine secretion. The application of iPSC-derived EVs imparted

Author contributions: Q.W., N.R., B.Z., K.M., U.B., and M.R. designed research; Q.W., N.R., K.T.W., S.O., P.A., E.Y.W., A.B., R.X.L., L.E.P.-E., S.M., E.V., B.F.L., and C.L. performed research; T.V. contributed new reagents/analytic tools; Q.W., N.R., K.T.W., J.B., J.S., S.O., P.A., A.B., Y.Z., T.R.N., R.X.L., C.Y.L., U.K., S.M., S.L., A.G., S.F., and U.B. analyzed data; and Q.W., K.T.W., S.O., P.A., E.Y.W., A.B., Y.Z., S.L., A.G., T.V., G.V.-N., B.Z., U.B., and M.R. wrote the paper.

Competing interest statement: Y.Z., G.V.-N., B.Z., and M.R. are inventors on patents for cardiac tissue cultivation that are licensed to Valo Health. Q.W., Y.Z., and M.R. have a filed patent application on thermoplastic polymer composition for micro 3D printing and uses thereof. B.Z. holds equity in OrganoBiotech.

This article is a PNAS Direct Submission. L.D.B. is a guest editor invited by the Editorial Board.

[1]To whom correspondence may be addressed. Email: m.radisic@utoronto.ca.

This article contains supporting information online at https://www.pnas.org/lookup/suppl/doi:10.1073/pnas.2403581121/-/DCSupplemental.

Published July 5, 2024.

cardioprotective effects in the presence of SARS-CoV-2, enabling the identification of miRNAs that facilitated functional improvements.

1. Results

1.1. Development of a Multiwell Heart-on-a-Chip Platform to Model Cardiac SARS-CoV-2 Pathogenesis and Therapeutic Screening. We developed a 3D-printed heart-on-a-chip platform, featuring 60 μm thermoplastic elastomer/quantum dot nanocomposite wires in microwells (19, 20). Human iPSC-derived cardiomyocytes and fibroblasts, combined with a collagen hydrogel, formed engineered cardiac tissue in these wells (Fig. 1*A*). Ang II was used as an independent factor to induce the progression of pathological cardiac dysfunction (13) (Fig. 1*A*). This system enables noninvasive, in situ monitoring of cardiac tissue function by measuring wire deflection during tissue contraction, which is optically tracked and quantified into contractile forces using calibration curves.

After 1 wk of tissue culture, the engineered cardiac tissue was fully compacted into a cylindrical strand, prompting the initiation of maturation conditioning with electrical stimulation (Fig. 1*B*). After an additional 2 wk, the tissues underwent a 1-h exposure to SARS-CoV-2 which was subsequently washed out, followed by tissue maintenance for another 2 wk with Ang II treatment (Fig. 1*B*). To study the efficacy of EVs as a potential therapy, they were introduced after SARS-CoV-2 infection (Fig. 1 *A* and *B*).

We used (phospho)proteomic analyses from our previous study (21) that identified 6,579 proteins and phosphorylation sites on 5,392 phosphoproteins in cardiac tissues and cross-referenced it to a published human protein interactome of SARS-CoV-2 proteins (22). Out of 266 proteins and 117 phosphoproteins (including ACE2) identified in our cardiac tissues interacting with SARS-CoV-2, 106 targets were identified in both proteomic and phosphoproteomic datasets (Fig. 1*C* and Dataset S1).

Immunoblotting for SARS-CoV-2 nucleoprotein (N) from infected iPSC-CMs (BJ1D) monolayer at an MOI 0.1 confirmed its elevated expression within 48 h, demonstrating that iPSC-CMs were permissive to SARS-CoV-2 infection (Fig. 1 *D* and *E*). iPSC-CMs from other sources (commercially available iCell cardiomyocytes) were also susceptible and permissive to SARS-CoV-2 infection (MOI 0.1; *SI Appendix*, Fig. S1). In longer infections (*SI Appendix*, Fig. S2*A*), extensive cytopathic effects were observed 5 days postinfection (dpi) (*SI Appendix*, Fig. S2*C*). To verify infection by SARS-CoV-2, median Tissue Culture Infectious Dose 50/mL ($TCID_{50}$/mL) was determined by tittering the supernatant from infected cardiomyocytes on Vero E6 cells, demonstrating an increase in TCID50/mL at 5 dpi (*SI Appendix*, Fig. S2*B*). We observed virus replication at a higher MOI 1 in the heart-on-a-chip model at 5 dpi, suggesting a minimum dose for the subsequent experiments in tissue models (Fig. 1*F*).

1.2. SARS-CoV-2-Induced Functional Decline in Cardiac Tissues. Transfecting dense tissues in the absence of vasculature for efficient mass transfer may be challenging; thus, a previous study (7) reported the use of an MOI 10. We tested several MOIs (0.1, 1, and 5) in the cardiac tissues. MOI 5 infection resulted in a reduced contractile force, decreasing rapidly at 5 to 7 dpi (Fig. 2*A* and *SI Appendix*, Fig. S3 *A–E*). MOI 0.1 and 1 did not lead to significant alterations in the tissue contractile behavior (*SI Appendix*, Fig. S3*E* and Fig. 2 *A–D*). All groups exhibited a comparable cytotoxicity (*SI Appendix*, Fig. S3*F*).

Excitation threshold (ET), a measure of electrical excitability, significantly increased in the MOI 5 group 1 wk after infection (Fig. 2*B*) and active force subsided to less than 10% of the force measured before infection (Fig. 2*C* and Movie S1). The active force to passive tension (AF/PT) ratio significantly declined in the MOI 5 group (Fig. 2*D*).

SARS-CoV-2 infection resulted in a loss of Ca^{2+} firing in the MOI 5 group, with only small areas of the tissue able to generate transients 1 wk after infection (Fig. 2*G* and Movie S3). In areas that retained the ability to generate Ca^{2+} transients, a decrease in Ca^{2+} amplitude was detected at both MOI 1 and 5 (Fig. 2*F*). Notably, the percentage of beating tissues was lower in the MOI 5 group (49.7%) 1 wk after infection, compared to all other groups (100%) (Fig. 2*H*). At MOI 5, the tissues did not exhibit a significant cell death, from live-dead staining (*SI Appendix*, Fig. S4), indicating an appropriate infection dose.

Immunofluorescence staining for F-actin and cardiac troponin T revealed the most elongated sarcomeric structure in control tissues, whereas sarcomere disruption and loss were consistently found in all SARS-CoV-2 infected groups, particularly notable at MOI 5 (Fig. 2*I* and *SI Appendix*, Fig. S5). F-actin and cardiac troponin T (cTNT) elongation, measured by the eccentricity parameter, were significantly disrupted in the MOI 5 SARS-CoV-2 infected tissues compared to the noninfected group, without a difference in F-actin density, indicating the disarrayed sarcomeres in infected tissues (Fig. 2 *J–L*). A gradual loss of cTNT was observed in infected tissues correlating with an increase in MOI (Fig. 2*N*).

TEM demonstrated sarcomere breakdown in SARS-CoV-2 infected tissues (*SI Appendix*, Fig. S6). Detection of budding and vesicle-bound virus-like particles (~80 nm-diameter circular structures) in the infected tissues next to the disrupted sarcomeres and notable vacuoles in the MOI 5 group were identified (*SI Appendix*, Fig. S6 *A* and *B*).

The amount of nuclear DNA fragmentation with TUNEL staining increased as a function of MOI 1 wk after infection, indicating increased apoptosis at higher viral doses (Fig. 2 *M* and *O*). The release of lactate dehydrogenase (LDH) was detected, related to necrosis, showing no significant difference among groups (Fig. 2*P* and *SI Appendix*, Fig. S3*F*).

One week after SARS-CoV-2 application, cytokine profiling revealed significantly increased levels of proinflammatory cytokines interleukin (IL)-6 (Fig. 2*Q*) and IL-8 (*SI Appendix*, Fig. S7*A*). IL-9, implicated in apoptosis prevention (23), was also elevated in MOI 1, but not in the MOI 5 group (Fig. 2*R*). Monocyte chemoattractant protein-1 (MCP-1), which regulates migration and infiltration of monocytes/macrophages, was significantly increased in infected tissues (Fig. 2*S*). Interestingly, SARS-CoV-2 infection also induced an elevation of platelet-derived growth factor-AA (PDGF-AA) known to be associated with vascular permeability (24) (Fig. 2*T*). Significant elevation in the chemokine secretion of regulated on activation, normal T cell expressed and secreted (RANTES) was detected in infected tissues, which is known to promote leukocyte infiltration to the sites of inflammation (25) (*SI Appendix*, Fig. S7*B*).

Common cold coronavirus HCoV-NL63 binds to the same receptor as SARS-CoV-2, ACE2, to enter host cells, whereas HCoV-229E uses a different receptor, aminopeptidase N (26, 27) that is extremely weakly expressed in the heart (28). No obvious difference was observed before and after common cold coronavirus infection as expected (*SI Appendix*, Fig. S8).

Principal component analysis (PCA) of RNA sequencing data indicated global expression changes associated primarily with SARS-CoV-2 infection with 78.32% variance with and without MOI 5 SARS-CoV-2 infection (Fig. 2*U*). The differential expression analysis (*SI Appendix*, Fig. S7*C*) revealed significantly activated pathways

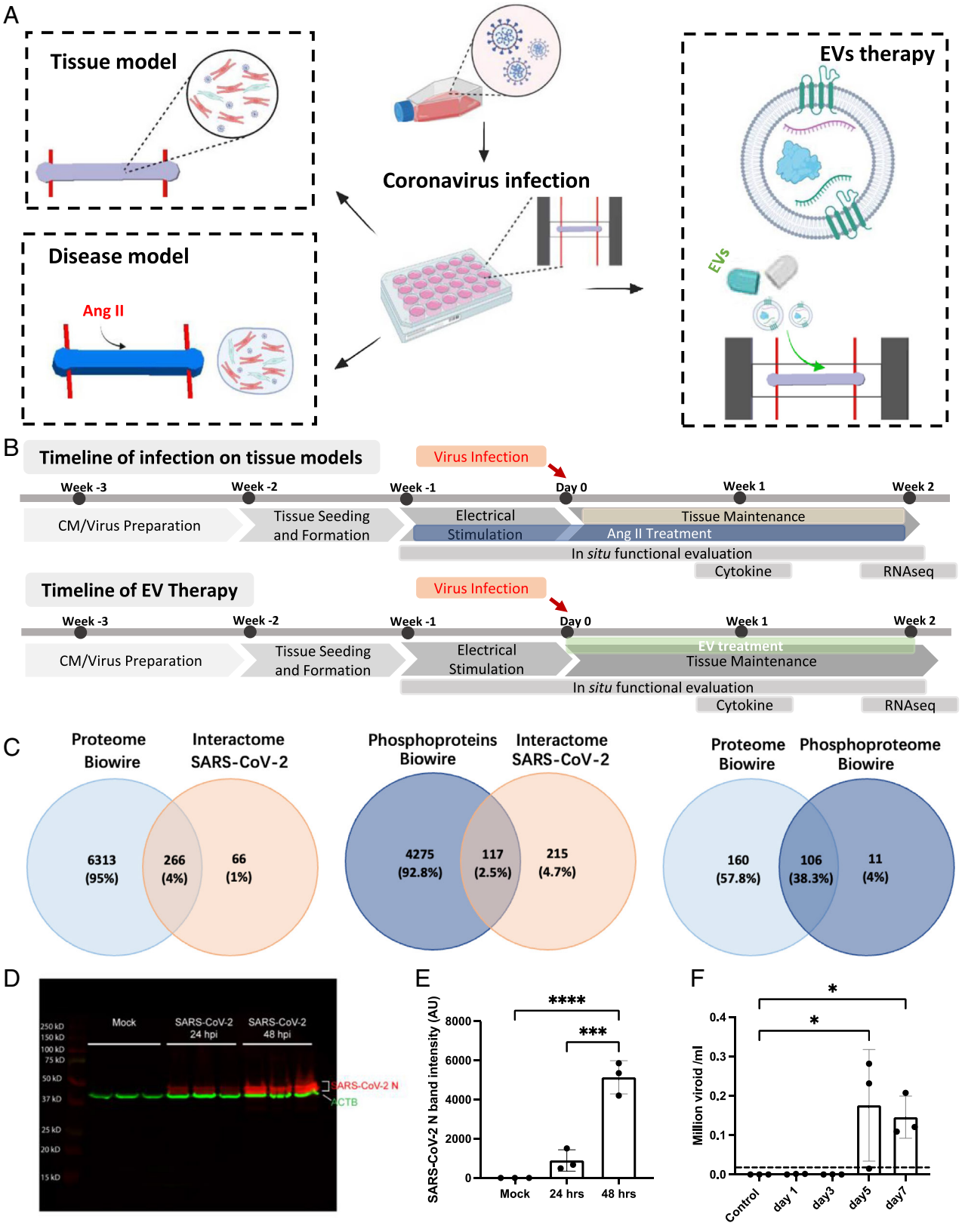

Fig. 1. Establishing heart-on-a-chip models to recapitulate SARS-CoV-2 pathogenesis in healthy and diseased myocardium for therapeutic screening. (*A*) Schematics of the healthy and Ang II–induced diseased cardiac tissue models in a multiwell platform that allows for SARS-CoV-2 application. Human iPSC-derived EVs were used for therapeutic screening. (*B*) The timeline shows the process of tissue formation, infection of tissue models with or without Ang II treatment and functional assessment, EVs treatment of the infected tissues without Ang II, functional readouts, and the analysis of cytokine release and mRNAseq. (*C*) Venn diagram of SARS-CoV-2 interactors identified in human iPSC-CM BJ1D cardiac Biowire II proteomic and phosphoproteomic datasets. (*D*) Western blot analysis of SARS-CoV-2 nucleoprotein in a cardiac monolayer culture using BJ1D human iPSC-CM (n = 3). Loading control is β-actin. (*E*) The intensity of SARS-CoV-2 N protein bands from western blot was measured by arbitrary units (AU) in mock and SARS-CoV-2 infected monolayer cultures at 24 h and 48 h after infection. (n = 3) *** indicates $P < 0.001$, and **** indicates $P < 0.0001$, one-way ANOVA. (*F*) qPCR performed on RNA extracted from SARS-CoV-2 (MOI 1)-infected tissues at various time points after infection. n = 3, * indicates $P < 0.01$ with control, one-way ANOVA. (Data are shown as average ± SD; n = 3, * indicates $P < 0.05$, and ** indicates $P < 0.01$ between Ang II–treated tissues and control by one-way ANOVA.)

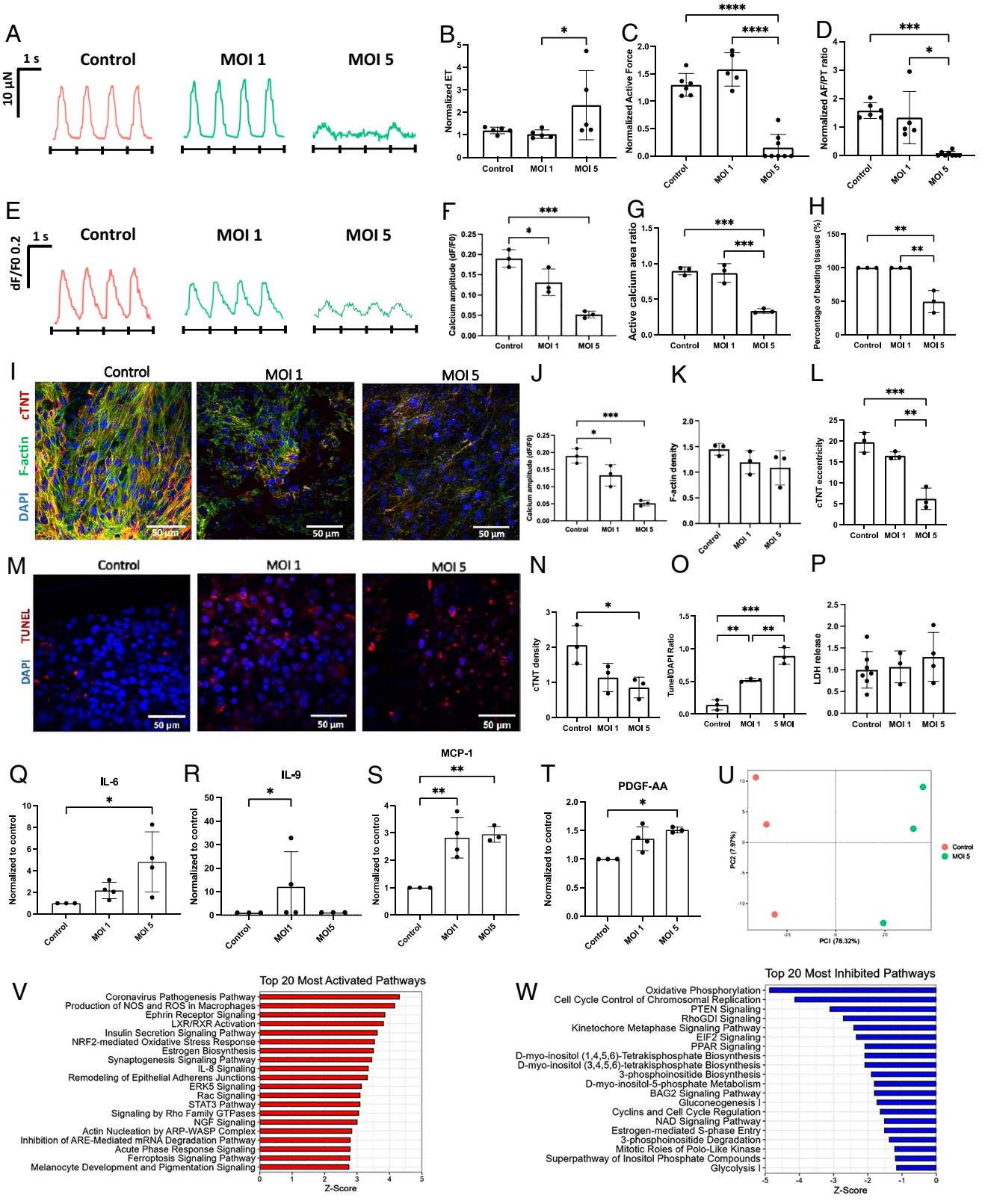

Fig. 2. SARS-CoV-2-induced functional decline of cardiac tissues. Noninfected controls and SARS-CoV-2-infected tissues at MOI 1 and 5 before and 1 wk after infection (*A*) Representative force traces recorded under 1 Hz electrical pacing. (*B*) The normalized ET. (*C*) The active force. (*D*) Active force to passive tension ratio, normalized to baseline values before infection for each tissue (n = 5 to 8). (*E*) Representative calcium traces (n = 3). Quantification of (*F*) calcium amplitude and (*G*) fraction of the tissue area with detectable Ca^{2+} transients (n = 3). (*H*) Percentage of beating tissues (three batches). (*I*) Immunostaining for sarcomeric-F-actin (green) and cardiac troponin-T (cTNT, red). Nuclei are counterstained with DAPI (blue) (n = 3). Quantification of eccentricity and density for (*J* and *K*) F-actin and (*L*) the eccentricity of cTNT. (*M*) Confocal images for nuclei DAPI (blue) and TUNEL (red) and (*O*) quantification of DNA fragmentation (TUNEL/DAPI) (n = 3). (*P*) LDH release in culture media (n = 3 to 7). Cytokine release: (*Q*) IL-6, (*R*) IL-9, (*S*) MCP-1, and (*T*) PDGF-AA, with values normalized to the control tissue (n = 3 to 4). (*U*) PCA of noninfected samples (control) and SARS-CoV-2 infected tissues (MOI 5) (n = 3/group). Pathway enrichment and activity analysis for control tissues compared with MOI5 infected tissues, showing top Z-scores (*V*) activated and (*W*) inhibited pathways via the Ingenuity Pathway Analysis (IPA) (n = 3/group). (All data from BJ1D human iPSC-derived cardiac tissues. Data are presented as mean ± SD; **P* < 0.05, ***P* < 0.01, ****P* < 0.001, and *****P* < 0.0001 indicate significant differences between each group, one-way ANOVA).

involved in coronavirus pathogenesis, inflammation, apoptosis, cardiac fibrosis, and stress response (Fig. 2*V*), whereas significantly inhibited pathways were related to cardiac metabolism (Fig. 2*W*).

1.3. Angiotensin II–Treated Cardiac Tissues Exhibit Higher Inflammation upon SARS-CoV-2 Infection. We further investigated how SARS-CoV-2 coronavirus impacted the cardiac function in a validated angiotensin II–induced disease model (13) (*SI Appendix*, Fig. S9 and *Supplementary Results*). The SARS-CoV-2 infection of Ang II–treated tissues resulted in reduced contractile forces (Fig. 3*A*). A significant increase in ET was observed in infected Ang II–treated tissues 2 wk after infection (Fig. 3*B*). Compared with the MOI 5 group, an earlier onset of contractile dysfunction was found in Ang II–treated tissues 3 d after infection (*SI Appendix*, Fig. S10 *A–D*), but no significant difference in contractile force 2 wk after infection (Fig. 3*C*). The AF/PT ratio significantly decreased in infected Ang II–treated tissues, compared to the Ang II group (Fig. 3*D*). Ang II treatment reduced contractility also at a lower viral dose of MOI 1 (*SI Appendix*, Fig. S10*E*), whereas MOI 1 Ang II–free tissues contracted comparably to the noninfected tissues.

The Ang II–treated SARS-CoV-2 tissues exhibited impaired Ca^{2+} transients comparable with the Ang II group alone and the MOI 5 group alone (Fig. 3 *E–G*). Fifty percent of the Ang II–treated tissues retained their ability to beat 2 wk after infection, comparable with the MOI 5 group and significantly lower than either control or Ang II alone tissues (Fig. 3*H*).

Tissues treated with Ang II presented sarcomere disruption 2 wk after infection (Fig. 3*I* and *SI Appendix*, Fig. S11). F-actin and cTNT elongation measured by the eccentricity parameter in the Ang II–treated tissues 2 wk after infection was lower than in the noninfected control group but higher than in the MOI 5 group (Fig. 3 *J* and *L*). We also observed less loss of cardiomyocytes (cTNT density) in the Ang II–treated group, compared to the MOI 5 group, with no obvious difference in F-actin density (Fig. 3 *K* and *N*). Apoptosis was significantly elevated compared to the control in both MOI 5 and Ang II–treated MOI 5 group, and it was significantly lower in the MOI 5 + Ang II group compared to the MOI 5 only group (Fig. 3 *M* and *O*). The level of LDH release in the media from the infected Ang II–treated tissues was higher than that of the control group 2 wk after infection, indicating increased necrosis due to Ang II treatment (Fig. 3*P*).

Ang II–treated tissue with SARS-CoV-2 application profoundly enhanced the secretion of classical inflammation markers IL-6 and IL-8 (Fig. 3*Q* and *SI Appendix*, Fig. S12*A*) and apoptosis-reducing IL-9 (Fig. 3*R*). Growth-regulated oncogene-alpha (GRO-α) (*SI Appendix*, Fig. S12*B*), a chemokine of activating neutrophils (29), monocyte chemoattractant MCP-1 (Fig. 3*R*), macrophage colony-stimulating factor (*SI Appendix*, Fig. S12*C*), and RANTES were significantly increased in Ang II–treated tissues (*SI Appendix*, Fig. S12*D*). Vascular endothelial growth factor A and PDGF-AA, both known to promote endothelial permeability, (*SI Appendix*, Fig. S12*E* and Fig. 3*T*) were also significantly enhanced due to Ang II treatment.

The ACE2 expression level from RNA sequencing was not affected by the Ang II treatment but declined 2 wk upon infection in MOI 5 and MOI 5 + Ang II group two (Fig. 3*U*). Viral RNA load in infected tissues at MOI 5 was significantly higher compared to noninfected tissues as expected, and it was not affected by Ang II treatment. (*SI Appendix*, Fig. S12*F*).

PCA indicated global expression changes associated primarily with SARS-CoV-2 infection and Ang II treatment (Fig. 3*V*). To identify genes and pathways associated with SARS-CoV-2 infection and Ang II treatment, a three-way Venn diagram presented 950 significant genes in MOI 5 + Ang II compared with control and Ang II treatment alone (Fig. 3*W*). Metabolism-related pathways were significantly activated in the group of MOI 5 + Ang II (*SI Appendix*, Fig. S12*G*). Differential expression analysis identified 18 significant (FDR < 0.05) genes in MOI 5 vs. MOI 5 + Ang II comparison (Fig. 3*X*). Ang II treatment further exacerbated signs of cardiomyopathy and fibrosis by modulating gene expression of factors like Insulin-Like Growth Factor Binding Protein 2, Calcium Voltage-Gated Channel Auxiliary Subunit Gamma 8, Proprotein Convertase Subtilisin/Kexin Type 6, Inter-Alpha-Trypsin Inhibitor Heavy Chain 4, and Macrophage Stimulating 1 known to be involved in cardiomyopathy, heart failure, and fibrosis (30–33) and down-regulating cell cycle marker B-cell Translocation Gene 3 which increases senescence (34) (Fig. 3*X*). Significant upregulation of genes related to Ang II activation via angiotensin II type 1 receptor (AT1R) in Ang II–treated infected tissues was confirmed (Fig. 3*Y*), including upregulation of Angiotensinogen (AGT) and Mitogen-Activated Protein Kinase 3 (MAPK3), implicated in the Ang II–dependent hypertension (35, 36). Interestingly, in the noninfected tissues, there was no effect of Ang II on AGT and MAPK3. When control and MOI 5 tissues were compared, there was an increase in AGT and MAPK3, as a result of the infection. Yet, when Ang II was applied in the context of infected tissues, AGT and MAPK3 increased even further.

1.4. iPSC-EVs for Potential Cardioprotective Effects. TEM images (Fig. 4*A*) indicated that the particles isolated from human iPSC (BJ1D) and differentiated CMs contained EVs, characterized by their classic cup-shaped morphology. Size distribution and concentration of isolated EVs were comparable between the two cell types (Fig. 4 *B–D*) and positive for EV marker proteins CD63 and ALIX (Fig. 4*E* and *SI Appendix*, Fig. S13 *A–D*). miRNA sequencing demonstrated a number of distinct and overlapping miRNA species in CM-EVs vs. iPSC-EVs (Fig. 4*F* and *SI Appendix*, Fig. S13*E*), which were clearly separated by PCA (Fig. 4*G*).

Treatment of hearts-on-a-chip with HCoV-NL63 resulted in a transient decrease in the active force, offering the opportunity for phenotypic screening of EVs (*SI Appendix*, Fig. S14). These initial screening experiments indicated that iPSC-EVs applied to the tissues 1 h after infection at a dose of 1.25×10^9 per tissue offered slight advantages in the recovery of contractile function over time compared to untreated HCoV-NL63 infected tissues and those treated with CM-EVs at the same dose (*SI Appendix*, Fig. S14), thus motivating the use of iPSC-EVs in further studies.

Focusing on the top 11 miRNAs differentially expressed between iPSC-EVs and CM-EVs, we performed miRNA target prediction in miRDB followed by Gene Ontology statistical overrepresentation analysis to identify enriched biological processes targeted by these miRNAs in EV-treated tissues (Fig. 4 *H–K*). The top 20 processes (Fig. 4*J*) targeted categories such as development, stress response, and metabolic processes. Since intracellular miRNAs usually suppress messenger RNA (mRNA) translation, potential means by which iPSC-EVs may improve contractile recovery of infected tissues are by reducing the effects of stress-responsive pathways (highlighted by the red bars) and modulating TGF-β signaling to improve cell survival and function (Fig. 4*J*). The Kyoto Encyclopedia of Genes and Genomes (KEGG) enrichment analysis, performed via miRPath, indicated that iPSC-EVs could benefit heart tissues by modulating Wnt and TGF-β signaling and through Hippo signaling regulation (Fig. 4*L*).

1.5. iPSC-EVs Promote Contractile Recovery in Heart-on-a-Chip upon SARS-CoV-2 Application. No significant difference was observed in the viral load between infected tissues with and without iPSC-EVs treatments, yet larger sample size may be warranted (*SI Appendix*, Fig. S15).

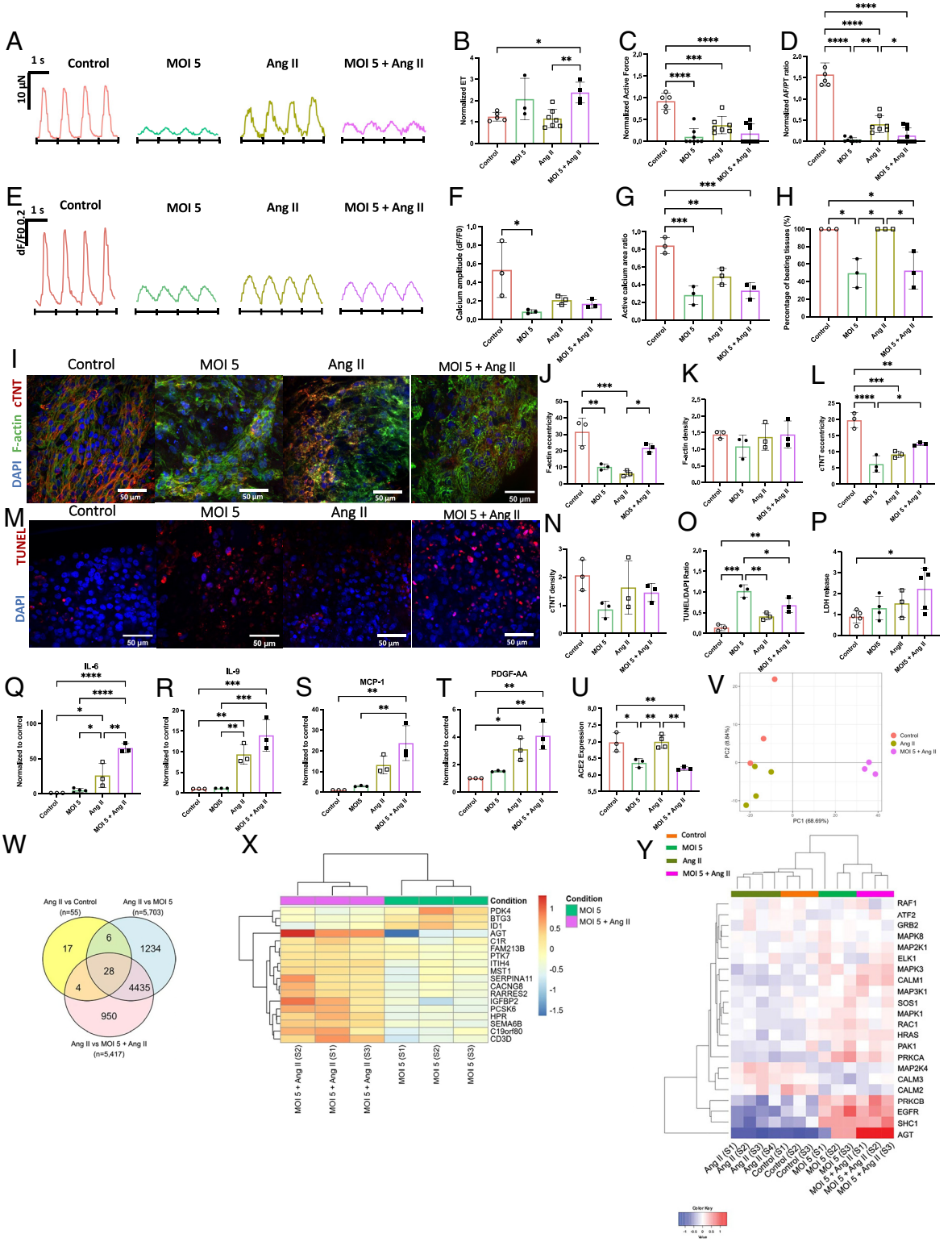

Fig. 3. Angiotensin II treatment leads to increased inflammation upon SARS-CoV-2 infection. Noninfected tissues (control), infected tissues at MOI 5 (MOI 5), noninfected tissue with Ang II treatment (Ang II), and infected tissues at MOI 5 with Ang II treatment (MOI 5 + Ang II) before and 2 wk after infection (*A*) Representative force traces recorded under 1 Hz electrical pacing. (*B*) The ET. (*C*) The active force normalized for each tissue to the baseline before infection. (*D*) The normalized active force to passive tension ratio (n = 5 to 9). (*E*) Representative calcium traces. Quantification of (*F*) calcium amplitude and (*G*) fraction of the tissue area with detectable Ca^{2+} transients. (*H*) Percentage of beating tissues (three batches). (*I*) Immunostaining for sarcomeric-F-actin (green) and cardiac troponin-T (cTNT, red). Nuclei are counterstained with DAPI (blue) (n = 3). Quantification of eccentricity and density for (*J* and *K*) F-actin and (*L* and *M*) cTNT was analyzed from the immunofluorescent images (n = 3). (*M*) Confocal fluorescent image stained for DAPI (blue) and TUNEL (red) (n = 3). Quantification of (*N*) the cTNT density and (*O*) DNA fragmentation (TUNEL/DAPI) (n = 3). (*P*) LDH release in culture media (n = 3 to 5). Cytokine release: (*Q*) IL-6, (*R*) IL-9, (*S*) MCP-1, and (*T*) PDGF-AA, with values normalized to the control group values (n = 3). (*U*) ACE2 from RNA sequencing (*$P < 0.05$ and **$P < 0.01$ indicate a significant difference between each group, one-way ANOVA, n = 3 to 4). (*V*) PCA. (*W*) Venn diagram of comparison of differentially expressed genes in control, MOI 5, Ang II, and MOI 5 + Ang II. (*X*) Gene expression heatmaps of differentially expressed genes associated with Ang II treatment of infected tissues, i.e., MOI 5 compared with MOI 5 + Ang II. n = 3. (*Y*) Gene expression heatmaps containing differentially expressed genes related to Ang II activation (BioCarta_AT1R_pathway) in control, MOI 5, Ang II, and MOI 5 + Ang II (n = 3). All data from BJ1D human iPSC-derived cardiac tissues. Data are shown as average ± SD; *$P < 0.05$, **$P < 0.01$, ***$P < 0.001$, and ****$P < 0.0001$ indicate significant differences between each group, one-way ANOVA.

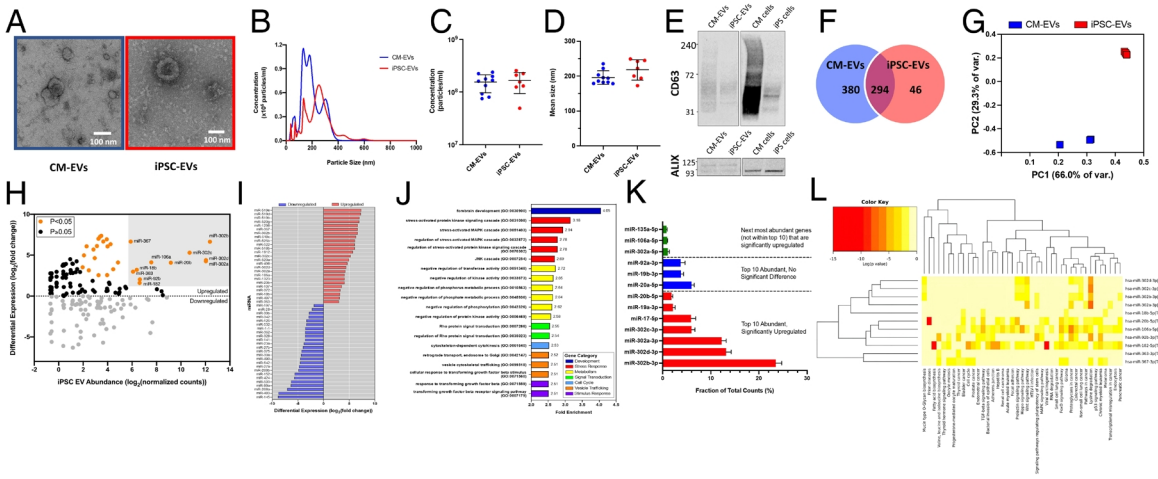

Fig. 4. Properties and miRNA composition of iPSC- and iPSC-CM-derived EVs. (*A*) TEM images of isolated CM- and iPSC-EVs. (Scale bar: 100 nm.) (*B*) Representative size distribution curves for EVs derived from BJ1D cardiomyocytes (CM-EVs) and stem cells (iPSC-EVs), measured via nanoparticle tracking analysis (NTA). (*C*) Particle concentration and (*D*) mean size of EVs. N = 10 for CM EVs and n = 7 for iPSC-EVs, Welch's *t* test. (*E*) Western blot detection of CD63 and ALIX, displayed alongside target detection in corresponding 2D cell culture lysates. (*F*) Comparison of the number of distinct vs. overlapping miRNA species detected in sequenced samples. (*G*) PCA. (*H*) Differential expression of miRNAs in iPSC-EVs, compared to CM-EVs, plotted against their relative abundance in iPSC-EVs. The top 12 most significantly up-regulated and most abundant miRNAs detected in iPSC-EVs are highlighted in the gray box and were selected for downstream target prediction and gene ontology analyses. (*I*) Top 25 significantly up-regulated and down-regulated miRNAs in iPSC-EVs with respect to CM-EVs. (*J*) Top 20 enriched gene ontology (GO) terms from the PANTHER GO-Slim biological process statistical overrepresentation test on predicted target genes derived from 9,812 abundant, up-regulated miRNAs in iPSC-EVs. Enriched GO terms represent potential processes that are significantly suppressed by iPSC-EVs miRNA cargo. (*K*) Fraction of total counts of different miRNA in iPSC-EVs, selected based on the total abundance and differential expression compared with those miRNAs in CM-EVs. (*L*) Heat map of the KEGG pathways in pathway enrichment analysis. For all miRNA sequencing figures: n = 3 for CM-EVs and n = 4 for iPSC-EVs. FDR-adjusted $P < 0.05$; FDR, false discovery rate.

iPSC-EVs-treated tissues (MOI 5 + EVs) showed maintenance of contractility and displayed significant recovery of active force at 5 dpi, in comparison to the MOI 5 tissues which gradually ceased contractility (Fig. 5 *A* and *C*, *SI Appendix*, Fig. S16, and Movie S1) with comparable ETs (Fig. 5*B*). The application of EVs alone had no impact on either ET or the active force (Fig. 5 *B* and *C*). AF/PT ratio in infected tissues significantly decreased, compared with the noninfected tissues with EVs or the controls (Fig. 5*D*). The AF/PT ratio of the MOI 5 + EVs group was significantly increased compared with that of the MOI 5 group alone, indicating force retention attributed to the administration of EVs (Fig. 5*D*). iPSC-EVs did not rescue the Ca^{2+} handling deficit in the infected tissues (Fig. 5 *E*–*G*). Infected tissues with iPSC-EVs treatment exhibited an enhanced percentage of beating tissues (90%) compared to the infected tissues without EVs treatment (49.7%) (Fig. 5*H*). In comparison to the control, EVs alone had no impact on either Ca^{2+} transients or the percentage of beating tissues (Fig. 5 *E*–*H*).

iPSC-EV treatment in SARS-CoV-2 infected tissues alleviated the loss of sarcomeric protein and nuclear staining (Fig. 5*I* and *SI Appendix*, Fig. S17). Significantly decreased F-actin and cTNT elongation were detected in the MOI 5 group (Fig. 5 *J* and *K*), with significant recovery of cTNT eccentricity upon iPSC-EVs treatment of the infected tissues (Fig. 5*K*). No significant difference in F-actin density was observed in all the groups, while cTNT density of the MOI 5 group was significantly decreased, compared to the noninfected tissues (Fig. 5 *M* and *N*), without reversal by the EV treatment. There was no impact of EVs alone on F-actin and cTNT density (Fig. 5 *M*–*N*). iPSC-EVs treated tissues exhibited reduced apoptosis, compared to infected tissues at MOI 5, and there was no impact in the absence of infection (Fig. 5 *L* and *O*). iPSC-EV treatment exhibited no significant impact on LDH release (Fig. 5*P*).

iPSC-EV treatment of infected tissues resulted in significantly reduced secretion of IL-4 (*SI Appendix*, Fig. S18*A*) and IL-1α (*SI Appendix*, Fig. S18*B*) and the enhanced secretion of IL-6 (Fig. 5 *Q*, *i*). A previous report (37) demonstrated that IL-6 exhibited varied roles, from heart protection to failure, indicating that the short-term IL-6 level can preserve the heart tissue while chronically increased IL-6 signaling was detrimental. Apoptosis preventing IL-9 (23) was elevated in iPSC-EVs-treated tissues (Fig. 5 *Q*, *ii*). GRO-α, a chemokine activating neutrophils (29), (*SI Appendix*, Fig. S18*C*) was significantly increased in iPSC-EVs treated infected tissues, compared with the MOI 5 group, and so were the MCP-1 and PDGF-AA (Fig. 5 *Q*, *iii* and *iv*). There was no impact of the EV treatment of noninfected tissues on inflammatory cytokine secretion, aside from IL-4 which was decreased with EV treatment (Fig. 5*Q* and *SI Appendix*, Fig. S18*A*).

Dose optimization may further be needed to improve the rescue of contractility. The infected tissues (MOI5) subjected to the multiple treatments (two doses per week) of iPSC EVs exhibited a significant increase in both active force and AF/PT ratio compared to the infected tissues without the treatment (Fig. 5 *R* and *S*). Yet, there was no significant difference in single and multiple doses at 1 wk, warrantying more systematic future investigation and longer term EV application.

PCA of mRNA sequencing data indicated that the first principal component accounts for 74.86% of the variance in gene expression and segregates samples infected with SARS-CoV-2 from tissues without infection. The second principal component (5.89%) and the third principal component (4.92%) appeared to represent expression differences associated with iPSC-EVs treatment (Fig. 5*T*). Differential expression analysis identified eight significant genes in the MOI 5 group vs. MOI 5 + EVs (Fig. 5*U*). The inflammation-related pathways were significantly activated in the MOI 5 group, and metabolism-related pathways were significantly activated in the MOI 5 + EVs group (Fig. 5*V*).

The therapeutic approach with iPSC-EVs decreased cell apoptosis and reduced signs of cardiac failure by reducing the expression of genes such as, glycogen phosphorylase, muscle associated (PYGM), and Zinc Finger Protein 330 (ZNF330) which are involved in cell death and apoptosis (38–41) (Fig. 5*W*) or by increasing the expression of Potassium Voltage-Gated Channel Interacting Protein 2 (KChIP2) and Secreted Frizzled Related Protein 2 (SFRP2) that enhanced excitability and reduced fibrosis (42, 43), respectively.

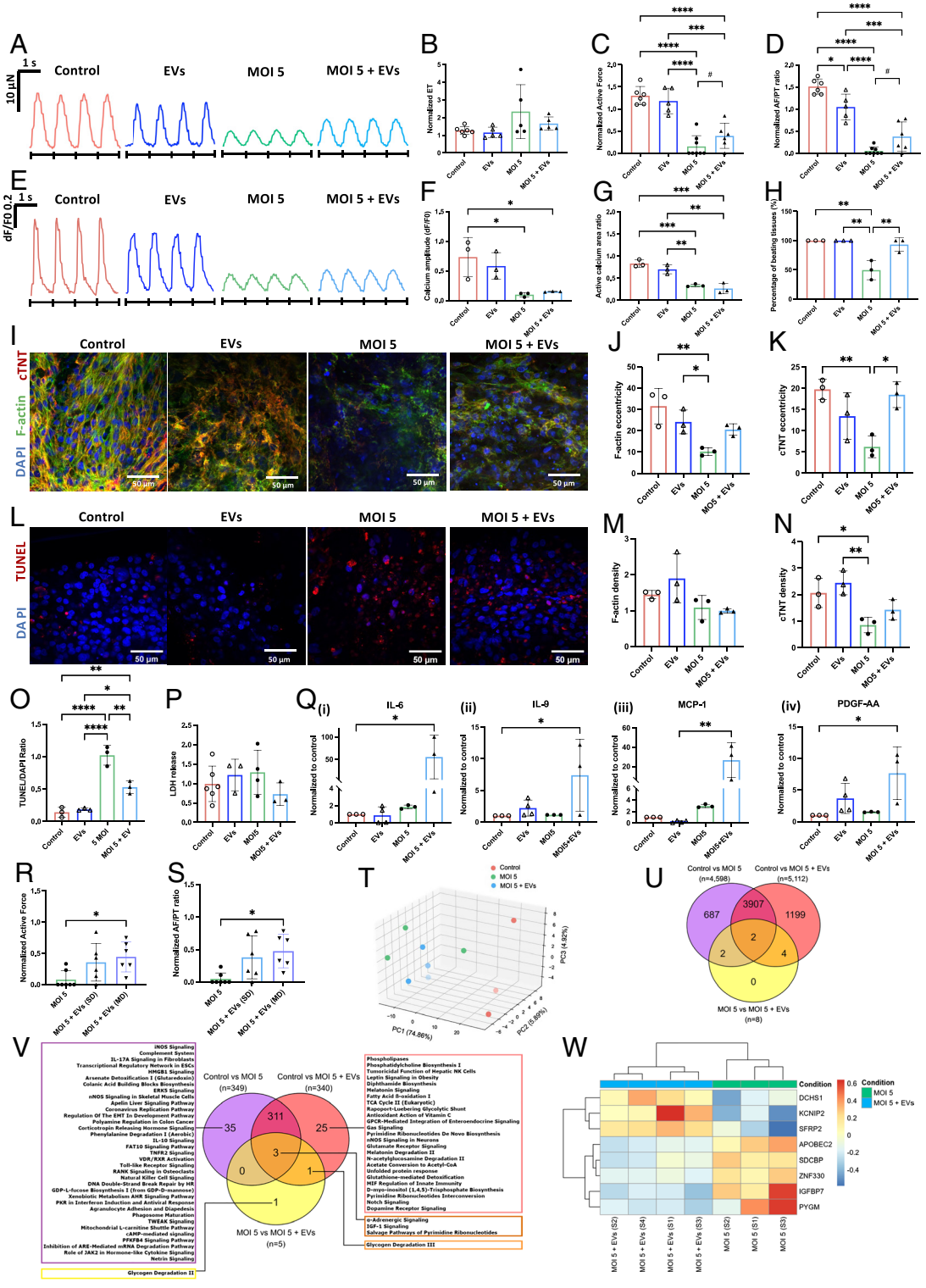

Fig. 5. Cardioprotective effects of iPSC-EVs in heart-on-a-chip. The figure shows the following groups: noninfected tissues without iPSC-EVs treatment (control group) and those with iPSC-EVs treatment (EVs group) as well as the infected tissues at MOI 5 without iPSC-EV treatment (MOI 5 group) and those with iPSC-EVs treatment (MOI 5 + EVs), 1 wk after infection. (*A*) Representative force traces recorded under 1 Hz stimulation. (*B*) Normalized ET. (*C*) The active force normalized for each tissue to the baseline before infection. (*D*) The normalized active force to passive tension ratio (n = 4 to 8). $^{*}P < 0.05$, $^{**}P < 0.01$, $^{***}P < 0.001$, and $^{****}P < 0.0001$ indicate significant differences between groups, one-way ANOVA. $^{\#}P < 0.05$ indicates a *t* test between MOI 5 and MOI 5 +EVs groups. (*E*) Representative calcium traces (n = 3). Quantification of (*F*) calcium amplitude and (*G*) fraction of the tissue area with detectable Ca^{2+} transients. (*H*) Percentage of beating tissues (three batches). (*I*) Immunostaining of sarcomeric-F-actin (green) and cardiac troponin-T (cTNT, red) 2 wk after infection. Nuclei are counterstained with DAPI (blue) (n = 3). Quantification of (*J*) F-actin eccentricity, (*K*) cTNT eccentricity (n = 3), (*L*) confocal fluorescent images stained for DAPI (blue) and TUNEL (red) (n= 3). Quantification of (*M*) F-actin density, and (*N*) cTNT density analyzed from the immunofluorescent images (n = 3). (*O*) Quantification of DNA fragmentation (TUNEL/DAPI) 2 wk after infection (n = 3). (*P*) LDH release in culture media (n ≥ 3). (*Q*) Cytokine release measured 1 wk after infection: *i*) IL-6, *ii*) IL-9, *iii*) MCP-1, and *iv*) PDGF-AA (n = 3). Normalized (*R*) active force and (*S*) AF/PT ratio compared among groups of infected tissues without (MOI 5) and with iPSC-EVs treatment from a single dose [MOI 5 + EVs (SD)] and multiple dose [MOI 5 + EVs (MD)] 1 wk after infection, normalized for each tissue to the baseline before infection (n = 6 to 7). (*T*) PCA of control, MOI 5, and MOI 5 + EVs 2 wk after infection (n = 3/group). (*U*) Venn diagram of differentially expressed genes and (*V*) activated pathways via IPA in control, MOI 5, and MOI 5 + EVs groups. (*W*) Gene expression heatmaps of differentially expressed genes for MOI 5 compared with MOI 5 + EVs groups. All data from BJ1D human iPSC-derived cardiac tissues. Data are shown as average ± SD; $^{*}P < 0.05$, $^{**}P < 0.01$, $^{***}P < 0.001$, and $^{****}P < 0.0001$ indicate significant differences between each group, one-way ANOVA.

Control vs. MOI 5 + EVs samples presented 1,203 genes (*SI Appendix*, Fig. S19*A*) and 26 pathways related to metabolism and facilitation of beta-oxidation suggesting a reduced reactive oxygen species formation in the iPSC-EV treated groups (*SI Appendix*, Fig. S19*B*). The 689 genes (*SI Appendix*, Fig. S19*A*) and 35 pathways (*SI Appendix*, Fig. S19*B*) that were enriched in control vs. MOI5 were mainly involved in inflammation.

1.6. Functional Role of Single miRNAs from iPSC-EVs in Cardiac Recovery. We individually administered miRNAs identified to be relevant to cardiomyocyte physiology and occurring in high abundance in the iPSC-EVs (Fig. 6 *A* and *C*) to cardiac monolayers followed by the SARS-CoV-2 application (Fig. 6*B*). Among the miRNAs investigated, miR-20a-5p (Fig. 6 *B* and *C*) was selected as it was abundant and could regulate genes that exhibited significant differential expression in the MOI 5 + EV compared to the MOI 5 group (Fig. 5*X*, SFRP2, ZNF330, PYGM, and DCHS1). miR-19a-3p and miR-302d-3p were selected as they exhibited abundance and a significant differential expression in iPSC-EVs compared to CM-EVs (Fig. 6*C*). Additionally, they have known functional impact on cardiomyocytes in terms of reducing apoptosis (44–46), protecting cardiac function (47–49), promoting proliferation, and repressing inflammation (50, 51).

After transfection with the fluorescent control, strong red fluorescent signals were observed in the cardiac monolayer, indicating the successful delivery of the transfection reagent (*SI Appendix*, Fig. S20). miRNA control (miR-mimic), a random sequence of miRNA, was also transfected to the infected monolayers and validated to not produce identifiable effects on contractility, F-actin, cTNT immunostaining, and apoptosis (*SI Appendix*, Fig. S21).

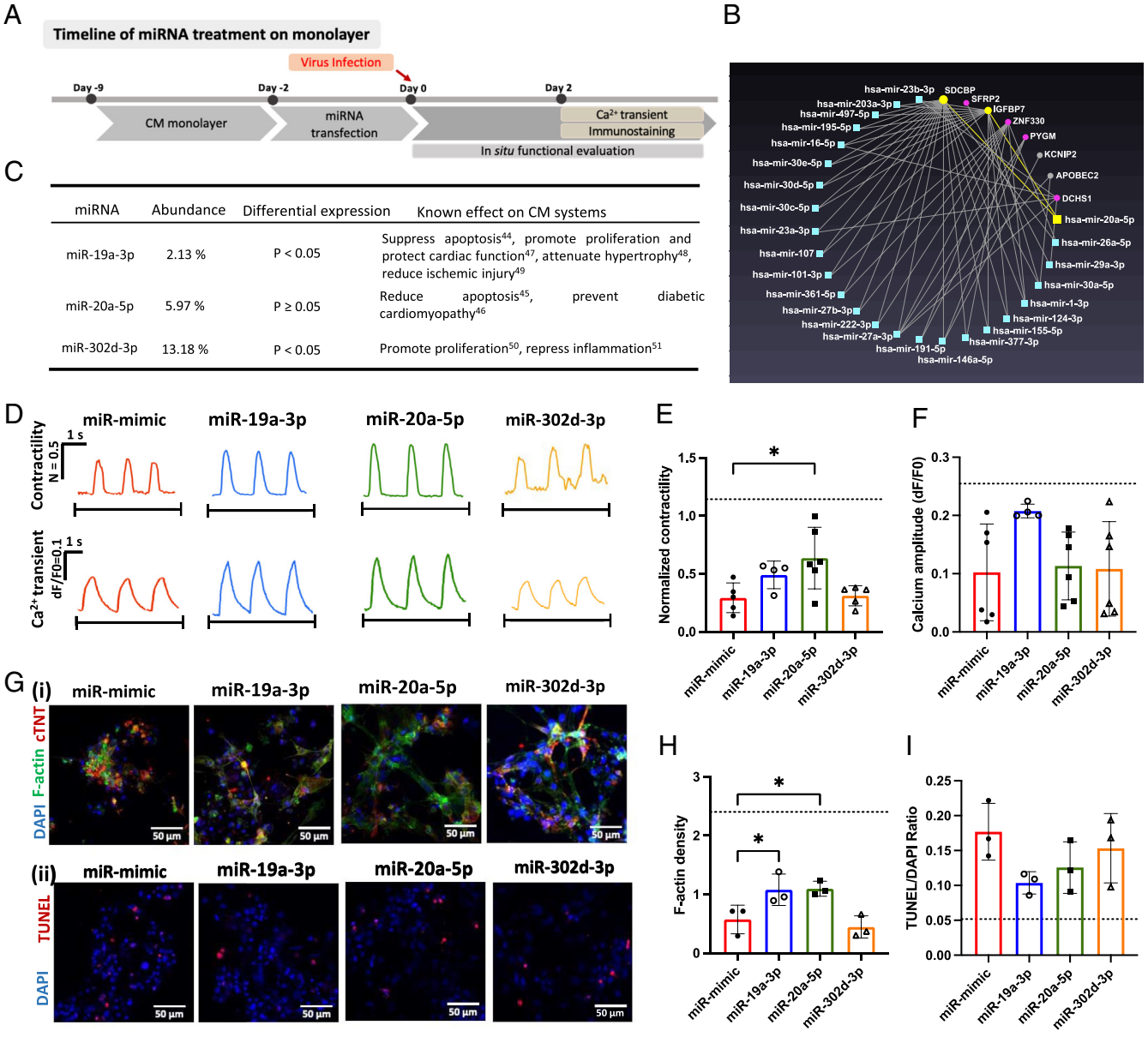

Fig. 6. Single miRNAs from iPSC-EVs can enhance cardiac recovery in the presence of SARS-CoV-2. (*A*) Experimental timeline. (*B*) Interaction among miR-20a-5p-target genes. (*C*) Target miRNA abundance in iPSC-EVs, their differential expression compared to those in CM-EVs, and their known effect in CM systems. iPSC-CM monolayers were transfected with miRNA mimic control (miR-mimic), miR-19a-3p, miR-20a-5p, and miR-302d-5p at MOI 0.1, exposed to SARS-CoV-2 and assessed at 2 dpi. (*D*) Representative contractility and calcium curves, contractility measured in AU. (*E*) Normalized contractility (n = 4 to 6). (*F*) Calcium amplitude (n = 4 to 6). [*G* (*i*)] Immunostaining for F-actin (green) and cardiac troponin T (red). Nuclei are counterstained with DAPI, (n = 3). Quantification of (*H*) F-actin density. [*G* (*ii*)] Confocal images with immunostaining of DAPI (blue) and TUNEL (red) and (*I*) quantification of DNA fragmentation (TUNEL/DAPI) (n = 3). The dashed lines in all bar figures indicate the corresponding values from the noninfected monolayer, without miRNA transfection. Data are shown as mean ± SD; **P* < 0.05 among those four groups, one-way ANOVA.

The transfection of miR-20a-5p significantly increased the contractility of the infected monolayer (Fig. 6 *D* and *E*), surpassing the effects observed with other miRNAs. No obvious differences in the calcium amplitude were observed among the infected monolayers after each miRNA transfection (Fig. 6 *D* and *F*). Increased F-actin densities, but not of cTnT (*SI Appendix*, Fig. S22), were observed in infected monolayers individually transfected with miR-19-3p and miR-20-5p, compared to the miR-mimic group, suggesting the potential recovery of the structural integrity (Fig. 6 *G*, *i* and *H*). No significant differences were observed in apoptosis (Fig. 6 *G*, *ii* and *I*), F-actin and cTNT eccentricity (*SI Appendix*, Fig. S22) between the groups.

2. Discussion

Hypertensive heart disease encompasses various abnormalities, notably left ventricular hypertrophy and both systolic and diastolic dysfunction (52). Hypertension and cardiomyopathy significantly amplify the risk of severe disease progression in COVID-19 (1–3). The underlying causes remain unclear, further compounded by the scarcity of models addressing these associations. This complexity necessitates models incorporating advanced high-content functional readouts.

We described previously a heart-on-a-chip disease model that captured progressive remodeling induced by Ang II (13). As a unique aspect, we assessed the effects of SARS-CoV-2 in this cardiac dysfunction model. We demonstrate the earlier onset of contractile dysfunction, loss of contractility at a lower viral dose, and a profoundly increased proinflammatory cytokine release, in line with hypertensive patients exhibiting an inflammatory predisposition before SARS-CoV-2 infection (53), all without differences in viral load. ACE2 expression was significantly decreased in infected tissues, regardless of Ang II stimulation. Half of the Ang II–treated infected tissues still retained their ability to beat 2 wk after infection, likely due to the known hypertrophic effects of Ang II that have compensatory effects on contractility over the short term (13).

Our model does not include immune and endothelial cells, such as neutrophils, eosinophils, T cells, monocytes, and macrophages, which are important for inflammation and immune responses. Yet, cardiomyocytes were previously reported to be the initiators of cardiac inflammation in nonischemic injury (54, 55) and together with cardiac fibroblasts can be activated to provide proinflammatory mediators (56), such as IL-6 (57, 58). We previously demonstrated the impact of immune cell inclusion in a blood vessel on a chip perfused with monocytes, resulting in ~100-fold upregulation of IL-6 and IL-8 upon SARS-CoV-2 exposure (59).

We also observed dramatic effects of endothelial EVs on contractility rescue in a vascularized cardiac muscle perfused with monocytes in the presence of SARS-CoV-2 (60). Yet, modeling of existing cardiac conditions such as hypertensive heart disease and studies of specific effects of single miRNAs warrant the initial investigation in simpler models, due to the complexity of parameters at play and the need to understand the effects on cardiomyocytes first.

Here, although iPSC-EVs helped maintain tissue contractility, they were unable to rescue Ca^{2+} transients, which may be related to Ca^{2+}-dependent membrane insertion by SARS-CoV-2 fusion peptide, possibly leading to a more profound disbalance of Ca^{2+} dynamics (61, 62). Our data do not rule out the possibility that EVs bind virus particles in the extracellular space, potentially preventing virus uptake. In such a case, the protective EV mechanism would extend beyond the effects if miRNAs in its cargo. The mesenchymal stem cell–derived EVs were reported to induce infected lung epithelial cells to suppress viral replication (63), whereas iPSC-EVs did not significantly impact viral replication here. The infected tissues subjected to multiple-dose treatment exhibited a significant recovery in contractile force compared to those receiving a single dose, which showed no difference from nontreated tissues, motivating further dose optimization studies.

Our data demonstrated the potential of iPSC-EVs to exert a cardioprotective effect against SARS-CoV-2 infection via the delivery of miRNAs to recipient cells. We focused on investigating the miRNAs which could regulate expression of genes we measured to be affected by the EV treatment (e.g., miRNA-20a-p for SFRP2, ZNF330, PYGM, DCHS1) as well as those with a known cardiac function and a significant differential expression in iPSC-EVs compared to CM-EVs. For example, miR-20a can reduce stress-induced cardiomyocyte apoptosis (46). miR-19a/19b enhanced cardiac functional recovery of myocardial infarction in a mouse model (64). Here, miR-19a-3p was observed to elevate the density of F-actin, showing the ability to maintain structural integrity, whereas miR-20a-5p improved both contractility and structural integrity of the infected CMs.

Taken together, our heart-on-a-chip models demonstrate SARS-CoV-2 pathogenesis under Ang II–induced cardiac dysfunction and suggest EV treatment and miRNA delivery as potential cardioprotective strategies against COVID-19-related myocardial injury.

3. Materials and Methods

3.1. Tissue Cultivation, Infection, and Characterization. SARS-CoV-2/SB2 infections on Biowires, cultivated as described previously (65) and in *SI Appendix*, were performed at a MOI 0.1-5 after 2 wk of tissue cultivation (66). Tissue functional properties, marker expression, and viability were assessed as we previously described and in *SI Appendix* (65).

3.2. EV Isolation and Characterization. Conditioned media were collected after 48 h of cultivation of undifferentiated BJ1D iPSC or differentiated cardiomyocytes. EV isolation and characterization were performed according to the previously described methods and as described in *SI Appendix* (67, 68).

Data, Materials, and Software Availability. All study data are available in the article, the *SI Appendix*, in GEO GSE185602 (69), ProteomeXchange PXD016492 (70), Mendeley (71) and by request from the Principal Investigator.

ACKNOWLEDGMENTS. This work is funded by the Canadian Institutes of Health Research (CIHR) Foundation Grant FDN-167274, Natural Sciences and Engineering Research Council of Canada (NSERC) Discovery Grant (RGPIN 326982-10), NIH Grant 2R01 HL076485, and NSERC Alliance Grant (ALLRP 5550), Killam Fellowship and Canada Research Chair (M.R.), CIHR and CRAFT postdoctoral awards (Q.W.), NSERC Postdoctoral Fellowship (A.B.), COVID-19 CIHR priority research grant (A.B. and K.M.), and Canada Foundation for Innovation/Ontario Research Fund (Project 19119 and 36442). Some components of schematics were created with BioRender.com. We acknowledge Felipe Jimenez Vargas and Dana Park for the help with data analysis. We acknowledge and thank the CRAFT facility, Donnelly Sequencing Centre and the C-CL3 Unit at the Temerty Faculty of Medicine, University of Toronto, as well as to the help of Prof. Gary Scott-Owen, Dr. Natasha Christie-Holmes, and Dr. Betty Poon.

Author affiliations: [a]Institute of Biomedical Engineering, University of Toronto, Toronto, ON M5S 3G9, Canada; [b]Toronto General Hospital Research Institute, University Health Network, Toronto, ON M5G 2C4, Canada; [c]Department of Chemical Engineering and Applied Chemistry, University of Toronto, Toronto, ON M5S 3E5, Canada; [d]Department of Mechanical and Industrial Engineering, University of Toronto, Toronto, ON M5S 3G8, Canada; [e]Department of Pediatrics, Section of Genomic Pediatrics, Medical College of Wisconsin, Milwaukee, WI 53226; [f]Department of Medicine, McMaster University, Toronto, ON L8S 4L8, Canada; [g]Vaccine and Infectious Disease Organization, Department of Veterinary Microbiology, University of Saskatchewan, Saskatoon, SK S7N 5E3, Canada; [h]Department of Biomedical Engineering, Columbia University, New York, NY 10027; [i]Department of Chemical Engineering, McMaster University, Hamilton, ON L8S 4L8, Canada; [j]Department of Physiology, University of Toronto, Toronto, ON M5S 1A8, Canada; [k]Ted Rogers Centre for Heart Research, University of Toronto, Toronto, ON M5G 1M1, Canada; [l]Medical Devices Research Center, Life Sciences Division, National Research Council Canada, Montreal, QC H4P 2R2, Canada; [m]Terrence Donnelly Centre for Cellular & Biomolecular Research, University of Toronto, Toronto, ON M5S 3E1, Canada; and [n]Department of Medicine, Columbia University, New York, NY 10032

1. K. J. Clerkin *et al.*, COVID-19 and cardiovascular disease. *Circulation* **141**, 1648–1655 (2020).
2. C. L. Bugert, V. Kwiat, I. C. Valera, J. J. Bugert, M. S. Parvatiyar, Cardiovascular injury due to SARS-CoV-2. *Curr. Clin. Microbiol. Rep.* **8**, 167–177 (2021).
3. Y. Xie, E. Xu, B. Bowe, Z. Al-Aly, Long-term cardiovascular outcomes of COVID-19. *Nat. Med.* **28**, 583–590 (2022).
4. L. Bao *et al.*, The pathogenicity of SARS-CoV-2 in hACE2 transgenic mice. *Nature* **583**, 830–833 (2020).
5. C. Muñoz-Fontela *et al.*, Animal models for COVID-19. *Nature* **586**, 509–515 (2020).
6. A. L. Bailey *et al.*, SARS-CoV-2 infects human engineered heart tissues and models COVID-19 myocarditis. *Basic Transl. Sci.* **6**, 331–345 (2021).
7. S. Marchiano *et al.*, SARS-CoV-2 infects human pluripotent stem cell-derived cardiomyocytes, impairing electrical and mechanical function. *Stem Cell Rep.* **16**, 478–492 (2021).
8. R. J. Mills *et al.*, BET inhibition blocks inflammation-induced cardiac dysfunction and SARS-CoV-2 infection. *Cell*, 2167–2182. e22 (2021).
9. R. M. Touyz, The role of angiotensin II in regulating vascular structural and functional changes in hypertension. *Curr. Hypertens. Rep.* **5**, 155–164 (2003).
10. Y. Liu *et al.*, Clinical and biochemical indexes from 2019-nCoV infected patients linked to viral loads and lung injury. *Sci. China Life Sci.* **63**, 364–374 (2020).
11. G. G. N. Serneri *et al.*, Cardiac angiotensin II formation in the clinical course of heart failure and its relationship with left ventricular function. *Circ. Res.* **88**, 961–968 (2001).
12. C. M. Ferrario, Role of angiotensin II in cardiovascular disease–Therapeutic implications of more than a century of research. *J. Renin Angiotensin Aldosterone Syst.* **7**, 3–14 (2006).
13. E. Y. Wang *et al.*, An organ-on-a-chip model for pre-clinical drug evaluation in progressive non-genetic cardiomyopathy. *J. Mol. Cell. Cardiol.* **160**, 97–110 (2021).
14. M. A. Sparks *et al.*, Severe acute respiratory syndrome coronavirus 2, COVID-19, and the renin-angiotensin system. *Hypertension* **76**, 1350–1367 (2020).
15. M. Khan *et al.*, Embryonic stem cell–derived exosomes promote endogenous repair mechanisms and enhance cardiac function following myocardial infarction. *Circ. Res.* **117**, 52–64 (2015).
16. M. Yadid *et al.*, Endothelial extracellular vesicles contain protective proteins and rescue ischemia-reperfusion injury in a human heart-on-chip. *Sci. Transl. Med.* **12**, eaax8005 (2020).
17. J. P. G. Sluijter *et al.*, Extracellular vesicles in diagnostics and therapy of the ischaemic heart: Position paper from the working group on cellular biology of the heart of the European society of cardiology. *Cardiovasc. Res.* **114**, 19–34 (2018).
18. K. T. Wagner, T. R. Nash, B. Liu, G. Vunjak-Novakovic, M. Radisic, Extracellular vesicles in cardiac regeneration: Potential applications for tissues-on-a-chip. *Trends Biotechnol.* **39**, 755–773 (2021).
19. Q. Wu *et al.*, Flexible 3D printed microwires and 3D microelectrodes for heart-on-a-chip engineering. *Biofabrication* **15**, 035023 (2023).
20. Q. Wu *et al.*, Automated fabrication of a scalable heart-on-a-chip device by 3D printing of thermoplastic elastomer nanocomposite and hot embossing. *Bioact. Mater* **33**, 46–60 (2024).
21. U. Kuzmanov *et al.*, Mapping signalling perturbations in myocardial fibrosis via the integrative phosphoproteomic profiling of tissue from diverse sources. *Nat. Biomed. Eng.* **4**, 889–900 (2020).
22. D. E. Gordon *et al.*, A SARS-CoV-2 protein interaction map reveals targets for drug repurposing. *Nature* **583**, 459–468 (2020).
23. A. M. Baird, R. M. Gerstein, L. J. Berg, The role of cytokine receptor signaling in lymphocyte development. *Curr. Opin. Immunol.* **11**, 157–166 (1999).
24. P. J. Keck *et al.*, Vascular permeability factor, an endothelial cell mitogen related to PDGF. *Science* **246**, 1309–1312 (1989).
25. R. Meurer *et al.*, Formation of eosinophilic and monocytic intradermal inflammatory sites in the dog by injection of human RANTES but not human monocyte chemoattractant protein 1, human macrophage inflammatory protein 1 alpha, or human interleukin 8. *J. Exp. Med.* **178**, 1913–1921 (1993).
26. C. L. Yeager *et al.*, Human aminopeptidase N is a receptor for human coronavirus 229E. *Nature* **357**, 420–422 (1992).
27. H. Hofmann *et al.*, Human coronavirus NL63 employs the severe acute respiratory syndrome coronavirus receptor for cellular entry. *Proc. Natl. Acad. Sci. U.S.A.* **102**, 7988–7993 (2005).
28. W. Wang, S. Lv, W. Gan, Z. Zeng, M. Yang, A bioinformatics analysis on the potential role of ACE2 in cardiac impairment of patients with coronavirus disease 2019. *Ann. Transl. Med.* **8**, 1403 (2020).
29. T. Geiser, B. Dewald, M. Ehrengruber, I. Clark-Lewis, M. Baggiolini, The interleukin-8-related chemotactic cytokines GRO alpha, GRO beta, and GRO gamma activate human neutrophil and basophil leukocytes. *J. Biol. Chem.* **268**, 15419–15424 (1993).
30. M. Barutaut *et al.*, Insulin-like growth factor binding protein 2 predicts mortality risk in heart failure. *Int. J. Cardiol.* **300**, 245–251 (2020).
31. A. Ortega *et al.*, Patients with dilated cardiomyopathy and sustained monomorphic ventricular tachycardia show up-regulation of KCNN3 and KCNJ2 genes and CACNG8-linked left ventricular dysfunction. *PLoS One* **10**, e0145518 (2015).
32. T. Kuhn *et al.*, Secretome analysis of cardiomyocytes identifies PCSK6 as a novel player in cardiac remodeling after myocardial infarction. *Circulation* **141**, 1628–1644 (2020).
33. H. Xu *et al.*, ITIH4: A new potential biomarker of "Toxin Syndrome" in coronary heart disease patient identified with proteomic method. *Evid. -Based Complementary Altern. Med.* **2013**, 360149 (2013).
34. T. Lin *et al.*, Loss of the candidate tumor suppressor BTG3 triggers acute cellular senescence via the ERK–JMJD3–p16 INK4a signaling axis. *Oncogene* **31**, 3287–3297 (2012).
35. J. R. Ingelfinger *et al.*, Rat proximal tubule cell line transformed with origin-defective SV40 DNA: Autocrine ANG II feedback. *Am. J. Physiol.-Renal Physiol.* **276**, F218–F227 (1999).
36. L. G. Navar, L. M. Harrison-Bernard, A. Nishiyama, H. Kobori, Regulation of intrarenal angiotensin II in hypertension. *Hypertension* **39**, 316–322 (2002).
37. J. A. Fontes, N. R. Rose, D. Čihák ová, The varying faces of IL-6: From cardiac protection to cardiac failure. *Cytokine* **74**, 62–68 (2015).
38. N. Wettersten, Biomarkers in acute heart failure: Diagnosis, prognosis, and treatment. *Int. J. Heart Failure* **3**, 81–105 (2021).
39. M. Migocka-Patrzałek, M. Elias, Muscle glycogen phosphorylase and its functional partners in health and disease. *Cells* **10**, 883 (2021).
40. C. Yarana *et al.*, Extracellular vesicles released by cardiomyocytes in a doxorubicin-induced cardiac injury mouse model contain protein biomarkers of early cardiac injury. *Clin. Cancer Res.* **24**, 1644–1653 (2018).
41. S. B. Mathiesen *et al.*, The cardiac syndecan-4 interactome reveals a role for syndecan-4 in nuclear translocation of muscle LIM protein (MLP). *J. Biol. Chem.* **294**, 8717–8731 (2019).
42. D. M. Nassal *et al.*, KChIP2 is a core transcriptional regulator of cardiac excitability. *Elife* **6**, e17304 (2017).
43. Y. Wu *et al.*, Multiple roles of sFRP2 in cardiac development and cardiovascular disease. *Int. J. Biol. Sci.* **16**, 730 (2020).
44. Z. Ma *et al.*, MiR-19a suppress apoptosis of myocardial cells in rats with myocardial ischemia/reperfusion through PTEN/Akt/P-Akt signaling pathway. *Eur. Rev. Med. Pharmacol. Sci.* **24**, 3322–3330 (2020).
45. X. Liu, B. Guo, W. Zhang, B. Ma, Y. Li, MiR-20a-5p overexpression prevented diabetic cardiomyopathy via inhibition of cardiomyocyte apoptosis, hypertrophy, fibrosis and JNK/NF-κB signalling pathway. *J. Biochem.* **170**, 349–362 (2021).
46. D. Frank *et al.*, MicroRNA-20a inhibits stress-induced cardiomyocyte apoptosis involving its novel target Egln3/PHD3. *J. Mol. Cell. Cardiol.* **52**, 711–717 (2012).
47. F. Gao *et al.*, Therapeutic role of miR-19a/19b in cardiac regeneration and protection from myocardial infarction. *Nat. Commun.* **10**, 1802 (2019).
48. Z.-J. Mao *et al.*, Shenfu injection attenuates rat myocardial hypertrophy by up-regulating miR-19a-3p expression. *Sci. Rep.* **8**, 4660 (2018).
49. M. Nasser *et al.*, Mesenchymal stem cell-derived exosome microRNA as therapy for cardiac ischemic injury. *Biomed. Pharmacother.* **143**, 112118 (2021).
50. F. Xu *et al.*, MicroRNA-302d promotes the proliferation of human pluripotent stem cell-derived cardiomyocytes by inhibiting LATS2 in the Hippo pathway. *Clin. Sci.* **133**, 1387–1399 (2019).
51. Y. Liu *et al.*, Mesenchymal stem cell-derived extracellular vesicle-shuttled microRNA-302d-3p represses inflammation and cardiac remodeling following acute myocardial infarction. *J. Cardiovasc. Transl. Res.* **15**, 754–771 (2022).
52. A. H. Gradman, F. Alfayoumi, From left ventricular hypertrophy to congestive heart failure: Management of hypertensive heart disease. *Prog. Cardiovasc. Dis.* **48**, 326–341 (2006).
53. S. Trump *et al.*, Hypertension delays viral clearance and exacerbates airway hyperinflammation in patients with COVID-19. *Nat. Biotechnol.* **39**, 705–716 (2021).
54. T. Suetomi, S. Miyamoto, J. H. Brown, Inflammation in nonischemic heart disease: Initiation by cardiomyocyte CaMKII and NLRP3 inflammasome signaling. *Am. J. Physiol. Heart Circ. Physiol.* **317**, H877–H890 (2019).
55. J. H. Brown, The contribution of the cardiomyocyte to tissue inflammation in cardiomyopathies. *Curr. Opin. Physiol.* **19**, 129–134 (2021).
56. D. Lindner *et al.*, Cardiac fibroblasts support cardiac inflammation in heart failure. *Basic Res. Cardiol.* **109**, 1–16 (2014).
57. K. Yamauchi-Takihara *et al.*, Hypoxic stress induces cardiac myocyte–derived interleukin-6. *Circulation* **91**, 1520–1524 (1995).
58. S. Fredj, J. Bescond, C. Louault, D. Potreau, Interactions between cardiac cells enhance cardiomyocyte hypertrophy and increase fibroblast proliferation. *J. Cell. Physiol.* **202**, 891–899 (2005).
59. R. X. Z. Lu *et al.*, Vasculature-on-a-chip platform with innate immunity enables identification of angiopoietin-1 derived peptide as a therapeutic for SARS-CoV-2 induced inflammation. *Lab Chip* **22**, 1171–1186 (2022).
60. R. X. Z. Lu *et al.*, Cardiac tissue model of immune-induced dysfunction reveals the role of free mitochondrial DNA and the therapeutic effects of exosomes. *Sci. Adv.* 10, eadk0164 (2024).
61. G. Khelashvili, A. Plante, M. Doktorova, H. Weinstein, Ca2+-dependent mechanism of membrane insertion and destabilization by the SARS-CoV-2 fusion peptide. *Biophys. J.* **120**, 1105–1119 (2021).
62. A. L. Lai, J. H. Freed, SARS-CoV-2 fusion peptide has a greater membrane perturbating effect than SARS-CoV with highly specific dependence on Ca2+. *J. Mol. Biol.* **433**, 166946 (2021).
63. S. Chutipongtanate *et al.*, Anti-SARS-CoV-2 effect of extracellular vesicles released from mesenchymal stem cells. *J. Extracell. Vesicles* **11**, e12201 (2022).
64. C. Chen, T. Chen, Y. Li, Y. Xu, miR-19a/19b improves the therapeutic potential of mesenchymal stem cells in a mouse model of myocardial infarction. *Gene Therapy* **28**, 29–37 (2021).
65. Y. Zhao *et al.*, A platform for generation of chamber-specific cardiac tissues and disease modeling. *Cell* **176**, 913–927. e18 (2019).
66. A. Banerjee *et al.*, Isolation, sequence, infectivity, and replication kinetics of severe acute respiratory syndrome coronavirus 2. *Emerg. Infect. Dis.* **26**, 2054 (2020).
67. K. T. Wagner, M. Radisic, A new role for extracellular vesicles in cardiac tissue engineering and regenerative medicine. *Adv. Nanobiomed Res.* **1**, 2100047 (2021).
68. B. Liu *et al.*, Cardiac recovery via extended cell-free delivery of extracellular vesicles secreted by cardiomyocytes derived from induced pluripotent stem cells. *Nat. Biomed. Eng.* **2**, 293–303 (2018).
69. Q. Wu *et al.*, Heart-on-a-chip model of SARS-CoV-2 infection and treatment with induced pluripotent stem cell derived extracellular vesicles. Gene Expression Omnibus. https://www.ncbi.nlm.nih.gov/geo/query/acc.cgi?acc=GSE185602. Deposited 9 October 2021.
70. U. Kuzmanov, A. Emili, Phosphoproteomic analysis of cardiac biowires, cardiac hypertrophy patient explants, and hypertrophic mouse heart. Proteome Xchange. https://proteomecentral.proteomexchange.org/cgi/GetDataset?ID=PXD016492. Deposited 28 November 2019.
71. Q. Wu, M. Radisic, SARS-CoV-2 pathogenesis in angiotensin II induced heart-on-a-chip disease model and extracellular vesicle screening. Mendeley Data. 10.17632/ssch7r4mjn.1. Deposited 21 June 2024.